Effect of Pre-deformation on Microstructure and Pitting Corrosion Behavior of UNS S32205

Xu Si, Jun Wu, Yiwei Tang, Jin Li, Yiming Jiang[*]

Department of Materials Science, Fudan University, Shanghai, 200433
[*]E-mail: ymjiang@fudan.edu.cn

The present work studied the microstructure of strain-induced martensite (SIM) in a UNS S32205 DSS under different strains. The material was strained at room temperature from 0 to 30% and the change of microstructure in the duplex stainless steel was investigated by several characterization techniques, such as optical metallographic microscopy (OMM), energy dispersive spectroscopy (EDS), scanning and transmission electron microscopy (SEM), X-ray diffraction (XRD), magnetic properties measurements and HV hardness measurements. In addition, the effects of the SIM on the corrosion behavior in chloride solutions with different pH have been studied. The experimental results showed that the SIM, the magnetization saturation and the micro-hardness values increased as the pre-tensile strain increased from 0 to 30%. The results also revealed that the pitting corrosion resistance was insensitive to the SIM. The pitting potential decreased in acid chloride solution at pH≈2 (3.5 wt.% NaCl+0.01 mol/L HCl) with the increasing of the deformation, however, in 3.5 wt.% NaCl solution and pH≈12(3.5 wt.% NaCl+0.01 mol/L NaOH), the pitting potential was hardly affected by the SIM.

1. INTRODUCTION

Duplex stainless steels (DSSs) consisting of approximately equal volume fractions of ferrite and austenite, are characterized by an attractive combination of greater mechanical properties and higher resistance to local corrosive attacks than the classical 300 series of austenite stainless grades[1-3]. Among DSSs, UNS S31803 (2205) with chromium (21-23 wt.%), molybdenum (2.5-3.5 wt.%), nickel (4.5-6.5 wt.%) and nitrogen (0.08-0.2 wt.%) is now a standard which has been widely used for the severe corrosion applications such as pulp and paper industry, chemical tankers, desalination plants [4,5]. Moreover, in order to meet the requirement of aggressive corrosion environments, UNS S32750 as a typical example of super duplex stainless steel with higher chromium (24-26 wt. %), molybdenum

(3.0-5.0 wt.%) and nickel (6.0-8.0 wt.%) as well as nitrogen (0.24-0.32 wt.%) shows greater strength and better corrosion resistance than ordinary duplex stainless steels, thus are widely used in high chloride environments, such as the marine and petrochemical industries [6]. However, due to the cost and price fluctuations of alloys, UNS S32101 with less chromium (21%-22 wt. %), molybdenum (0.1-0.8 wt.%), nickel (1.35-1.7 wt.%) and nitrogen (0.20-0.25 wt.%) has been developed as a typical lean DSS. It is increasingly used in nuclear plant and building structure thanks to its higher yield strength, better pitting corrosion resistance but lower cost than 304 austenite stainless steel [7,8].

A number of studies on the plastic deformation effects in austenite stainless steels have been reported [9-12]. It is found that plastic deformation gives rise to structural refinement and martensite transformation [13,14]. Recently, transformation induced plasticity (TRIP) effect has been studied extensively in duplex stainless steels in order to improve the greater ductility [15]. The TRIP mechanism is based on deformation-stimulated displacive transformation of metastable austenite to martensite, which remarkably improves both strength and ductility of the stainless steel. The SIM formation is related to many parameters, such as temperature, strain rate and stacking fault energy (SFE). Marco et al. [16] have proposed that the austenite-to-SIM is related to the stability of retained-austenite and the stacking fault energy (SFE). The austenite-to-SIM transformation was frequently found in lean DSSs in virtue of their lower SFE and the stability of retained-austenite than the higher-alloyed DSSs such as UNS S32205 DSS. Guo et al. [17] have revealed the characteristic of SIM in the 2002 DDS under different strains and the effect of SIM on different aspects. It is generally believed that TRIP occurred in austenite with the SFE less than 20 mJ/m^2. The empirical typical equation calculating SFE for stainless steels proposed by Schramn et al[18].

$$SFE(mJ/m^2) = -53+6.2\%Ni+0.7\%Cr+3.2\%Mn+9.3\%Mo \quad (1)$$

Recently Guo et al. [17] have reported that the sequence of martensitic transformations in UNS S32002 DSS is $\gamma \rightarrow \varepsilon \rightarrow \alpha'$ under the strain deformation. Sudipta et al. [19] have also examined the martensite transformed in UNS S32205 DSS under cold rolling.

Duplex stainless steels are widely used in marine environments because of their good resistance to the pitting corrosion. Pitting corrosion of stainless steel is one of the most dangerous forms of local corrosion. The corrosion resistance of duplex stainless steel relates to the alloy content, heat treatment, pH and the microstructure etc. There are papers reporting the influence of phase on the pitting corrosion of stainless steel. For example, Tsai et al. [20] have revealed the selective dissolution of constitution phases in mixed H_2SO_4/HCl solutions under different potentials. Alvarez et al. [21] studied the corrosion behaviour of two corrugated lean duplex stainless steels (SAF 2001 and 2304 grades) in eight alkaline solutions (carbonated and non-carbonated, saturated $Ca(OH)_2$ solutions with different chloride contents). Guo et al. [17] have reported that the pitting corrosion resistance was insensitive to the SIM and the SIM effect on pitting corrosion both in neutral and acid solutions.

With consideration of previous researches, the way of retaining austenite transforms to martensite in UNS S32205 DSS, the corrosion resistance affected by the SIM is still ambiguous. Therefore, the key point of this paper is to investigate the characteristic of the SIM and the properties induced by the SIM, such as micro-hardness, magnetic properties and pitting corrosion behaviors. More specifically, this study used optical metallographic microscopy (OMM), energy dispersive spectroscopy (EDS), scanning electron microscopy (SEM), transmission electron microscopy (TEM),

X-ray diffraction (XRD), magnetic properties measurements, HV hardness measurements to analysis the change of microstructure, the corrosion resistance was investigated by several electrochemical measurements.

2. EXPERIMENTAL

The material for examinations was delivered in the form of sheet-cutting steel with dimensions about 250 mm × 30mm × 1.5 mm. The chemical composition of the duplex stainless steel UNS S31803 was shown in Table 1. Then samples were subjected to pre-tensile ranging from 5%, 10%, 15%, 20% to 30%, using an Instron 5985 testing machine according to BS EN ISO6892-1:2009. The uniaxial tensile tests were conducted at room temperature at a strain rate of 3 mm/min. Rectangular specimens with a dimension of 10 mm × 10 mm were cut from these tensile specimens for further study. The specimens were solution treated at 1050°C for 1h in an arc furnace, then followed by water quenching to obtain the best mechanical and corrosion resistance properties.[22, 23]. Metallographic specimens were etched in a Beraha reagent (20 mL hydrochloric acid, 80 mL distilled water, and 0.3 g potassium metabisulfite). The white region in Fig.1 corresponds to the austenitic phase (γ) while the gray region is the ferritic phase (α). The microstructure was observed using optical metallographic microscopy (OMM) and scanning electron microscopy (SEM, Philips XL 30 FEG) after etching procedure. The major alloying elements in the individual phases were analyzed by energy dispersive spectroscopy (EDS, Philips XL 30 FEG) and were shown in Table 2.

Table 1. Chemical composition of the sample (wt.%)

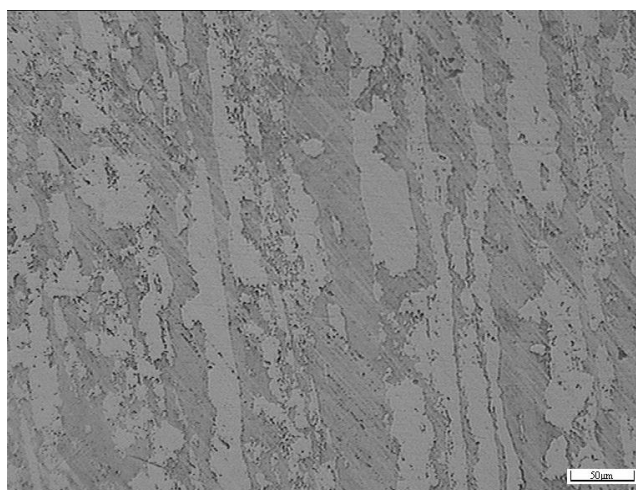| Element	C	Si	P	S	Cr	Ni	Mo	N	Mn	Cu
Wt.%	0.016	0.43	0.03	0.002	22.46	5.39	3.11	0.18	1.57	0.25

Figure 1. Microstructure of the specimen

Measurements of the magnetization saturation were performed in a vibrating sample magnetometer (Quantum Design, USA). The micro hardness with 100g was measured in a HMV-2TADW micro-hardness tester (Shimadzu Corporation, Japan). The ferrite detector measurements were repeated in at least ten different fields on the surface of the same specimen, and the average data was calculated as the volume fraction values of ferromagnetic phase.

X-ray diffraction tests were carried out through a D8 ADVANCE X-ray diffractometer with DAVINCI. DESIGN (Bruker Corporation, Germany) using Cu Kα (λ=0.154056 nm) radiation and operated at 40 kV and 20 mA, in the step-scan mode with a step size of 0.01°. The diffraction spectra have a 2θ angular range from 40 to 120°.

The electrochemical tests were performed with a CHI660D workstation (Shanghai Chenhua Instrument Co., Ltd, Shanghai, China). The corrosion test consisted of critical pitting temperature (CPT) test according to ASTM G 150-99 [22] and potentiodynamic polarization curve measurement according to ASTM G 59-97 [23]. All the potentials were measured with respect to a saturated calomel electrode (SCE) as a reference electrode, a platinum slice was used as the counter electrode. CPT test was conducted in solution of l mol/L NaCl via potentiostatic electrochemical method by applying a constant potential of 750 mV and increasing the solution temperature at a constant rate of 1℃/min from 2℃. The corresponding current was recorded simultaneously as the temperature increased during the test. The experiment was terminated when the current density reached 100 µA/cm^2 and kept surging for 1min. The temperature at which the current density was 100 µA/cm^2 was recorded as a CPT.

The pitting potential was identified as the potential at which the current density continuously exceeded 100 µA/cm^2. To avoid the crevice corrosion, interfaces between specimen and resin were sealed with silica gel sealant and dried in air. The exposed electrode surface area was 10mm^2. The test solution was prepared with analytical grade reagent and distilled water. Before and during the test, pure nitrogen gas (N_2) was passed into the electrolyte to get rid of the oxygen gas (O_2) for 30 min and maintained throughout the test. Potentiodynamic polarization curve measurements were conducted in the solution of 3.5 wt.% NaCl, 3.5 wt.% NaCl+0.01 mol/L HCl and 3.5 wt.% NaCl+0.01 mol/L NaOH at 60℃ with a scan rate of 0.1667 mV/s from -0.8 V versus SCE to the pitting potential ($E_{pit.}$) versus SCE. In addition, before the CPT and the potentiodynamic polarization measurement, cathodic polarization at -900 mV versus SCE for 2min was employed to deoxidize the surface of the working electrode, followed by stabilization at open circuit potential for 30min. Each type of electrochemical testing was repeated at least six times, and the average data were chosen as the CPT and E_{pit} values in this work.

3. RESULT AND DISCUSSION

Fig.1 shows the optical microstructure of the DSS as received etched by the Beraha. It exhibits a very good contrast between the light and dark regions. The volume fractions of the dark and light phases evaluated by using Image Tool software, were 0.53±0.02 and 0.47±0.03, indicating that the amount of austenite was the same as the amount of ferrite in content. The observation of specimens by

means of SEM with backscattered electron was presented in Fig.2. The major alloying elements of the bipolar phases were analyzed using energy dispersive spectroscopy (EDS) which were listed in Table 2.
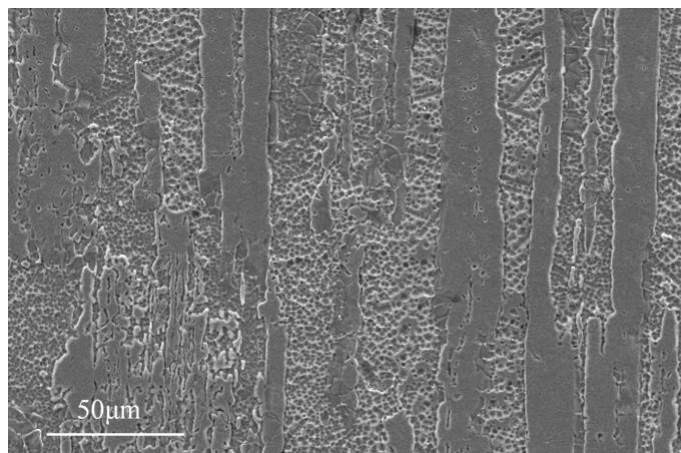

Figure 2. SEM morphologies of the specimen before deformation

Table 2. EDS results of the major alloying elements (wt.%) of martensite and austenite phase in UNS S32205 DSS

Element	Cr	Ni	Mn	Mo
Ferrite	23.92	4.49	1.91	5.99
Austenite	20.93	7.15	2.37	3.15

The susceptibility to deformation induced martensite transformation increase with the decrease of SFE. When the value of SFE < 18 mJ/m^2 and the molar Gibbs energy of the martensite reaction $\gamma_{fcc} \rightarrow \alpha'^{Ms}_{bcc}$ is negative, martensite formation—either ε-martensite by $\gamma_{fcc} \rightarrow \varepsilon^{Ms}_{hcp}$ or, for even lower SFE's, α'–martensite formation by $\gamma_{fcc} \rightarrow \varepsilon^{Ms}_{hcp} \rightarrow \alpha'^{Ms}_{bcc}$—becomes the favored transformation mechanism that affects the further deformation of the material[24-26]. According to calculation of equation (1), the SFE of UNS S31803 was about 30 mJ/m^2. But this equation was applied for austenite stainless steel. Therefore, it needs to be further explored whether the SIM in the UNS S32205 after the strain deformation.

Fig. 3 presents the microstructure of the UNS S32205 with the deformation of 5%, 10%, 15%, 20% and 30% by SEM. The observation indicated that there were some new lath-type phases that appeared inside the austenite. Meanwhile, the number of the lath-type phases rose with the increasing of the deformation. However, it was difficult to precisely distinguish martensitic lathes from deformation twin crystals and quantitatively measure the martensitic volume fraction by SEM.
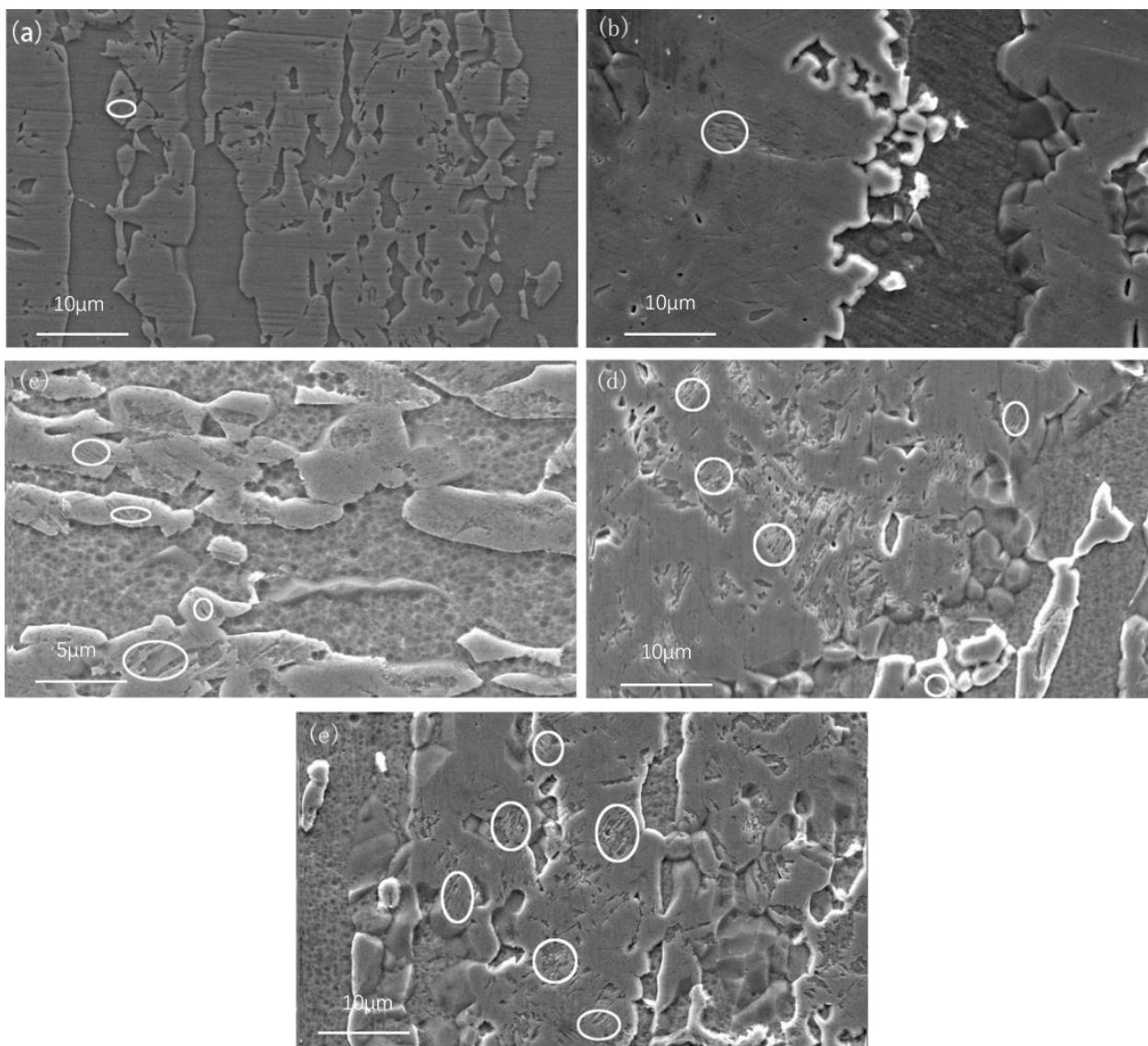
Figure 3. Microstructure of the specimens after different pre-tensile deformations (a) 5%, (b) 10%, (c) 15%, (d) 20%, (e)30%

Fig.4 presents the X-ray diffraction of the specimens with different strain deformations of 5%, 10%, 15%, 20%, 30%. The peaks of ferrite, austenite and martensite were clearly visible. It could be seen that the (111), (200), (220) and (311) diffraction peak intensity of the FCC austenite (γ) decreased as the strain increased from 0 to 30%. The (220), (211) diffraction peaks of the α'-martensite and δ-ferrite increased as the strain increased from 0 to 30%. This phenomenon was attributed to the conversion of austenite to martensite. Nevertheless, the peak width increased with the increasing of the deformation which may be ascribed to the grain refinement. In addition, the diffraction peaks of ε-martensite were not found in any deformation specimens.
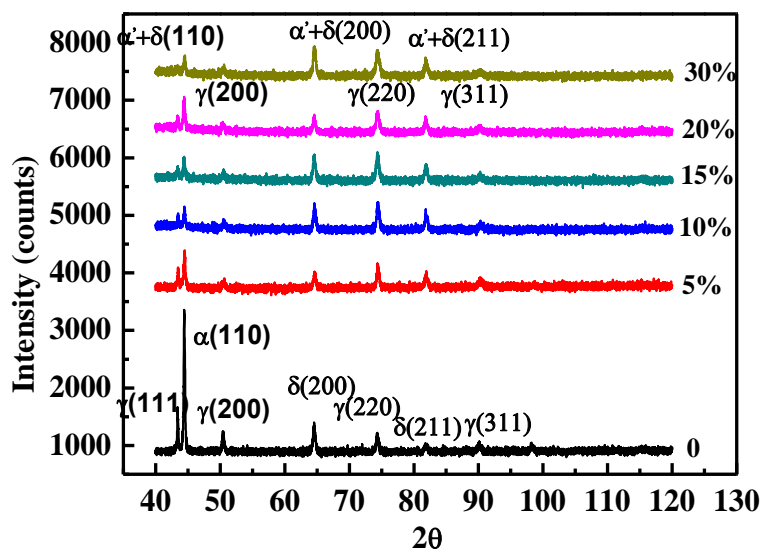
Figure 4. X-ray diffraction patterns samples subjected to the different strain.
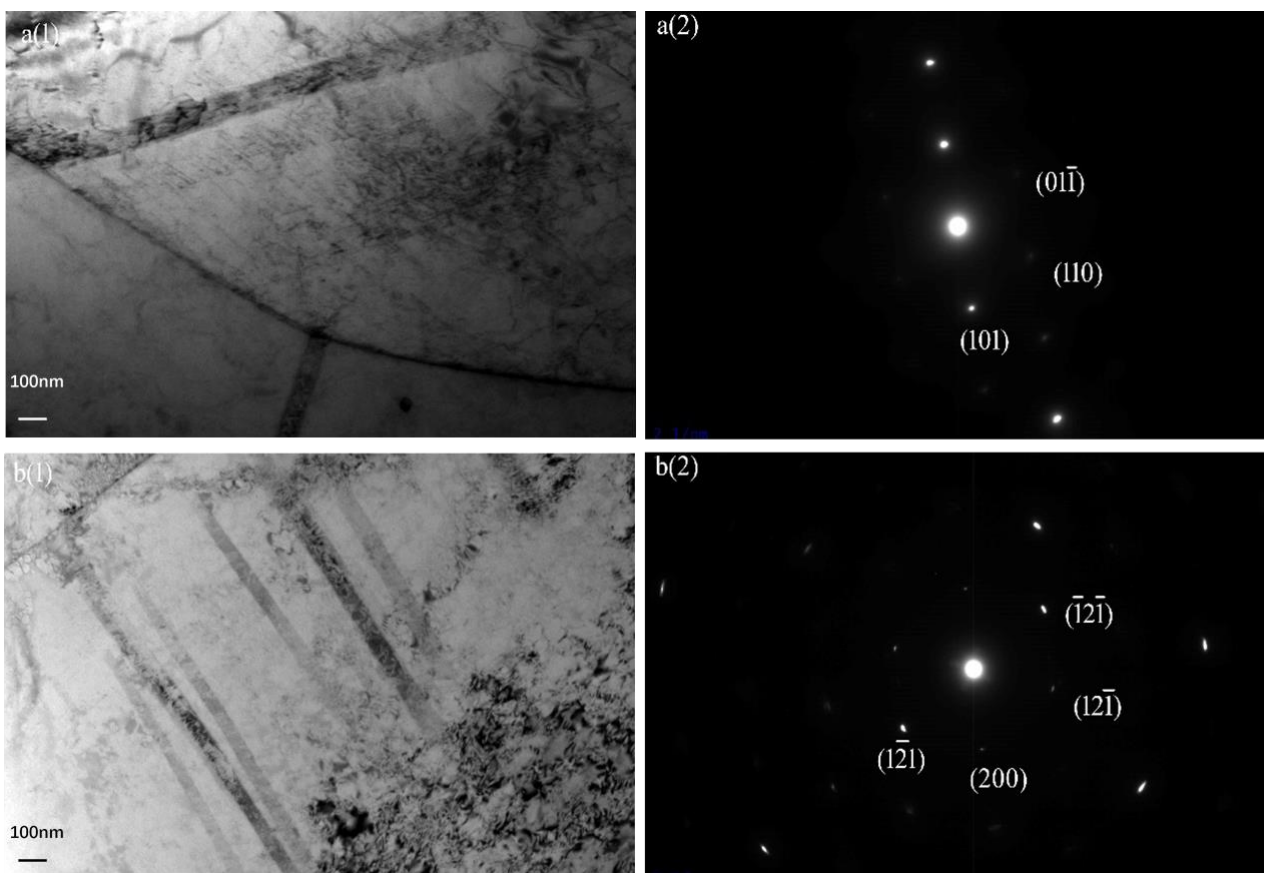

Figure 5. TEM micrographs of the specimens deformed at different strains (a)5%, (b)30%

The further analysis of the martensite formation was conducted by TEM. The TEM micrograph of the specimens under 5% and 30% pre-tensile were shown in Fig. 5. The TEM characterization of specimens deformed to 5% and 30% was revealed in Figs. 5a-b and Figs. 5c-d respectively. Fig. 5a and

Fig. 5c exhibited the presence of SIM as dark phase and austenite as bright phase. It was easy to find out that the SIM were generated in austenite grains. Moreover, the orientation relationship of strain induced ε-martensite was not detected by SEM as well as the XRD patterns, which might be a consequence of the higher SFE.

As we all know, the ferrite and α'-martensite were ferromagnetic phase, so the quantification of SIM could be realized by the magnetic saturation measurements. Figs. 6a-b display magnetization curves and magnetization saturation of the specimens with different tensile strains. As can be seen in these figures, the magnetization saturation increased with strain deformation increased from 0 to 30% of samples. This was due to the formation of the SIM ($\gamma \rightarrow \alpha'$) and the value of SIM increasing with the deformation.
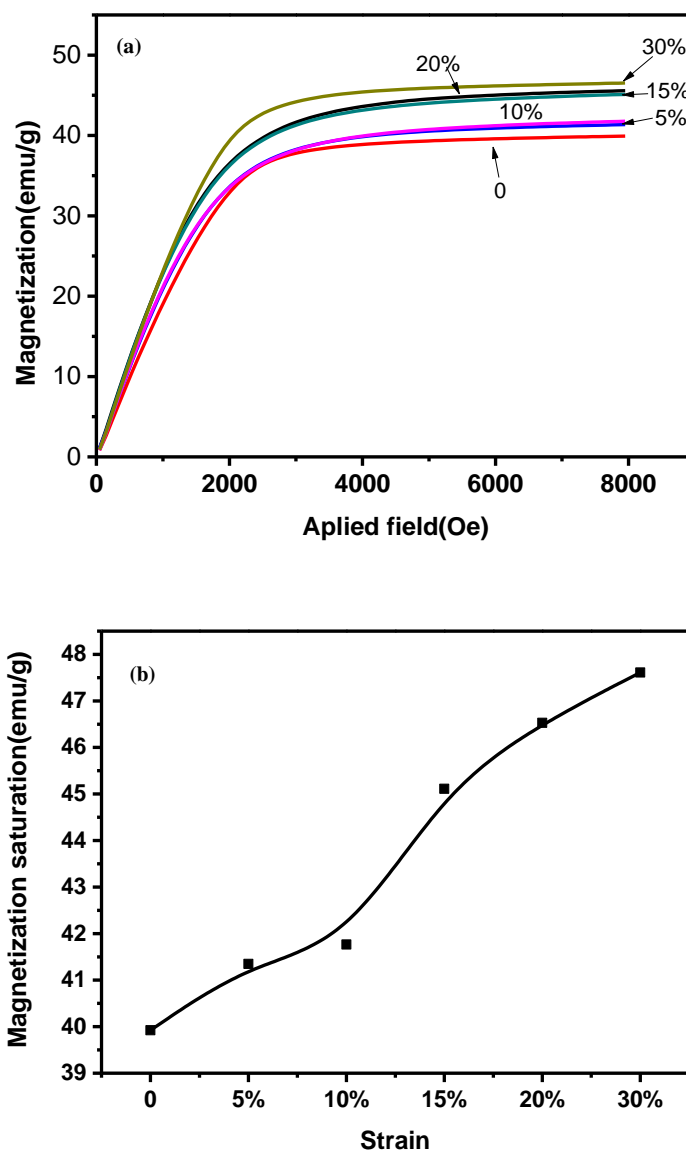

Figure 6. (a) Magnetization curves of the specimens with different tensile strains (b) Magnetization saturation with different tensile strains

Fig.7 exhibits the variation of the micro hardness with the deformation. By comparing the Fig. 6(b) and Fig. 7, a similar linear relationship between them can be found. From the figures, it was clearly observed that the Vickers hardness increased with the increasing of the strain from 240 to 337. This phenomenon could be caused by the formation of SIM which had higher hardness than austenite or ferrite.
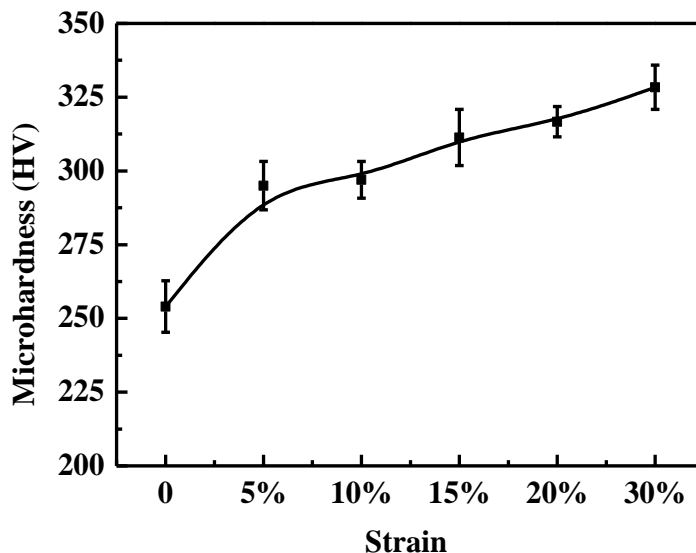

Figure 7. HV hardness with different pre-tensile strains with different tensile

The critical pitting temperature of materials is a significant parameter for the corrosion resistance. Figs.8-9 illustrate the CPT of specimens under different deformations by applying 750mV vs SCE in 1 mol/L NaCl deaerated neutral solution initially at 0°C. After an initial temperature stabilization period (the surface of samples was protected by the passivation film and the current density presented a numerical value less than $1\mu A/cm^2$), the solution was heated at a constant speed of 1 °C/min.
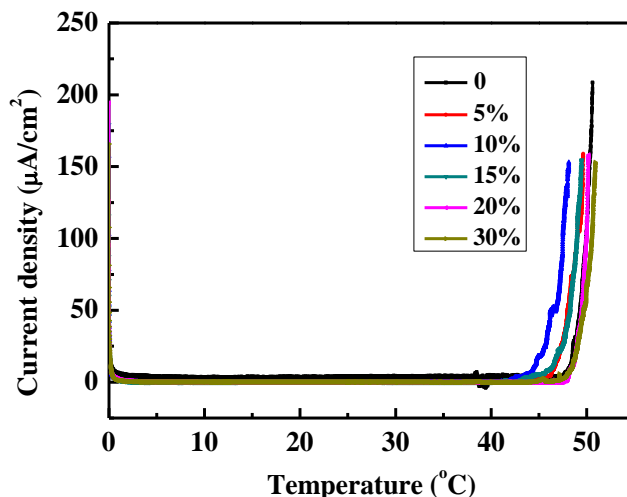

Figure 8. Curves of current density and temperature for the specimens with different pre-tensile strains in 1 M NaCl solution at an applied potential of 700 mV versus SCE

The current is monitored during the temperature scan, and the CPT is defined as the temperature at which the current increases rapidly (passive film breakdown). However, for practical reasons the CPT was recorded as the temperature at which the current density exceeds 100 $\mu A/cm^2$ for 60s during the tests. Fig. 9 shows the numerical values of the CPT derived from different deformations were very close. Besides, the fluctuation range of the CPT had not gone beyond 4 °C. The CPT testing results manifested that the SIM did not affect CPT value of the UNS S32205 DDS.
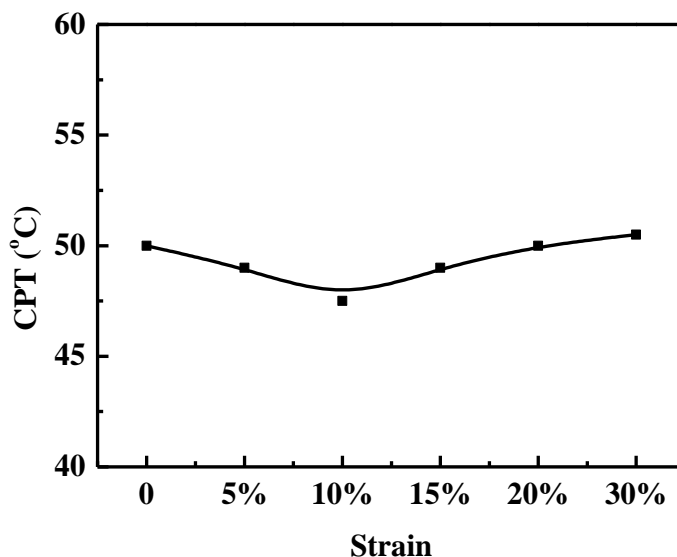

Figure 9. The average CPT values of specimens with different tensile strains

The cathodic Tafel constant (β_c), anodic Tafel slope (β_a), corrosion potential and corrosion current density according to the polarization curve were fitted with the software provided by the CHI660D potentiostation. The result of potentiodynamic polarization obtained in pH≈2 solution (3.5 wt.% NaCl + 0.01 mol/L HCl) at 60 °C (above the CPT acquired by Fig. 8) was presented in Fig. 10. The polarization curves exhibits that the strain deformation's impacted the corrosion behavior of the UNS S32205 DDS. The fitted corrosion parameters achieved by the polarization curves were presented in the Table 3. It is well-known that the material is less stable with negative corrosion potential (E_{corr}) and it is generally more prone to suffer serious corrosion. However, the material would suffer less attack if it applied with positive potential. On the other hand, the material with lower pitting potential was more susceptible to the pitting corrosion. In acid solution curves, it was clearly observed that the passive current density nearly had no change and the length of the passive regions of the polarization curves decreased with the increasing of the deformation. Besides, both the undeformed and deformed specimens exhibited similar corrosion potential. However, with the strain deformation increasing from 0 to 30%, the E_{pit} decreased from 317mV to 262mV. These results indicate that the SIM influenced the corrosion resistance of samples in the acid solution and the high local dislocation density might contribute to the weakness of the corrosion resistance. Besides, the test results of E_{pit} suggested that the corrosion resistance of UNS S32205 decreased with the increasing of strain deformation. It was noteworthy that the passive current did not change with the increasing of the deformation.
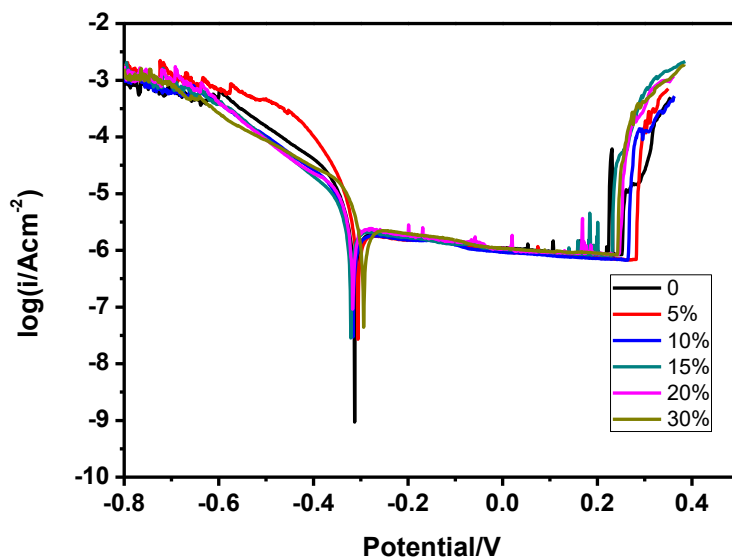
Figure 10. Potentiodynamic polarization curves for the specimens with different pre-tensile strains in 3.5 wt.% NaCl+0.01 mol/L HCl solution (pH≈2)

Table 3. Corrosion parameters of the samples studied in 3.5 wt.% NaCl+0.01 mol/L HCl solution

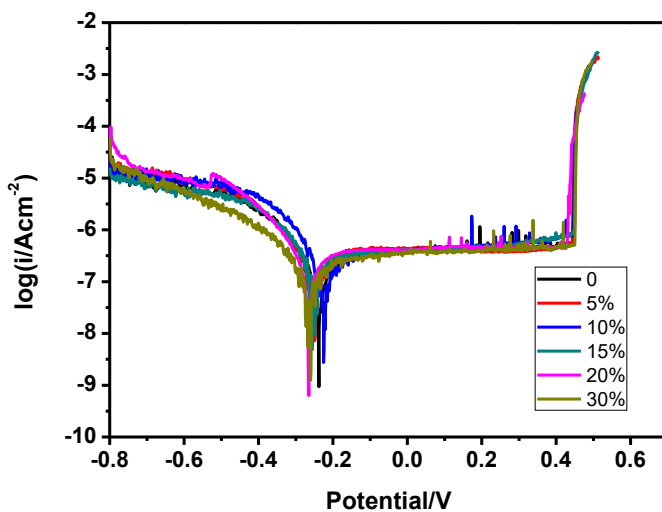| Sample-strain	β_c (V/dec)	β_a (V/dec)	E_{corr}(mV)vs. SCE	$\log(i_{corr})$ (A cm^{-2})	$\log i_p$ (A cm^{-2})	E_{pit} (mV) vs. SCE
0%	0.154	1.175	-317	-5.07	-6.07	317
5%	0.131	1.199	-308	-5.24	-6.17	296
10%	0.171	0.863	-318	-5.11	-6.15	284
15%	0.151	0.991	-321	-5.03	-6.06	268
20%	0.224	1.260	-318	-4.83	-6.07	267
30%	0.234	0.871	-301	-4.91	-6.07	262

Figure 11. Potentiodynamic polarization curves for the specimens with different pre-tensile strains in 3.5 wt.% NaCl solution (pH=7)

Table 4. Corrosion parameters of the samples studied in 3.5 wt.% NaCl solution

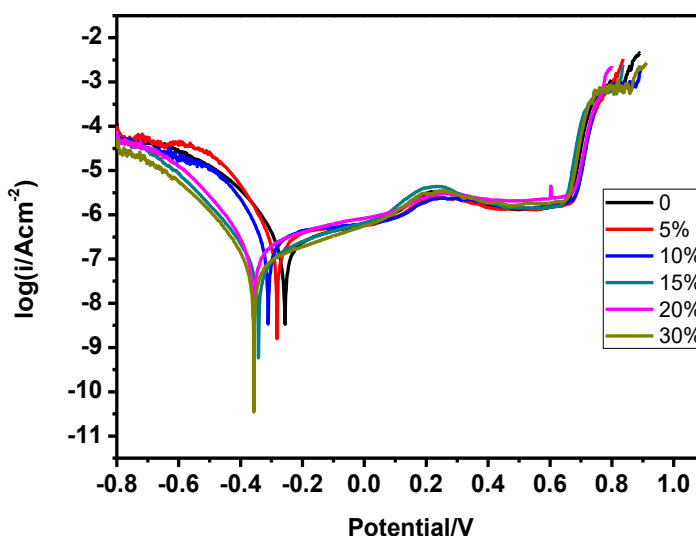| Sample-strain	β_c (V/dec)	β_a (V/dec)	E_{corr}(mV)vs. SCE	$\log(i_{corr})$ (A cm^{-2})	$\log i_p$ (A cm^{-2})	E_{pit} (mV) vs. SCE
0%	0.120	0.507	-244	-6.56	-6.34	454
5%	0.113	0.545	- 257	-6.32	-6.41	451
10%	0.123	0.565	-236	-6.44	-6.26	452
15%	0.134	0.572	-256	-6.59	-6.29	455
20%	0.107	0.562	-267	-6.47	-6.34	452
30%	0.137	0.594	-268	-6.58	-6.37	456

Figure 12. Potentiodynamic polarization curves for the specimens with different pre-tensile strains in 3.5 wt.% NaCl +0.01 mol/L NaOH solution (pH≈12)

Table 5. Corrosion parameters of the samples studied in 3.5 wt.% NaCl +0.01 mol/L NaOH solution

Sample-strain	β_c (V/dec)	β_a (V/dec)	E_{corr}(mV)vs. SCE	$\log(i_{corr})$ (A cm^{-2})	$\log i_p$ (A cm^{-2})	E_{pit} (mV) vs. SCE
0%	0.104	0.342	-260	-6.69	-5.77	841
5%	0.111	0.248	-282	-6.56	-5.84	780
10%	0.096	0.266	-314	-6.56	-5.75	893
15%	0.108	0.245	-345	-7.07	-5.71	821
20%	0.108	0.281	-359	-6.79	-5.65	776
30%	0.107	0.299	-359	-7.13	-5.73	868

Fig. 11 exhibits the polarization curves which reflected the pitting corrosion behavior of the specimens in neutral solution after different pre-strains tensile. The corresponding corrosion parameters were listed in Table 4. As could be seen in Table 4, both the undeformed and deformed specimens exhibited similar pitting potential (E_{pit}). Meanwhile, the corrosion potential with different strain deformation did not change obviously. This was in conformity with the CPT results, which

suggests that SIM had no obvious influence on the pitting corrosion resistance of the specimens in neutral chloride solution.

The result of potentiodynamic polarization obtained in the alkaline solution was presented in Fig.12. The corresponding corrosion parameters were listed in Table 5.

In contrast with the corrosion parameters in different solution, it was easily found that the Tafel slops didn't change obviously under the same pH. However, the values of Tafel slopes varied differentially in the solution under different pH. The different values of cathodic Tafel slope (β_c) suggested that the different mechanism of cathodic reaction occurred in different solution (hydrogen evolution in acid chloride solution, oxygen reduction reaction in acid and neutral chloride solution) [27]. Therefore, it could be found that the values of cathodic Tafel slope were similar both in acid and neutral chloride solution. Moreover, the values of anodic Tafel slope (β_a) increased with the decreasing of pH in chloride solution. It therefore needs some other corrosion parameters to discuss the corrosion situation.

The E_{pit} of samples under the same deformation increased with the increasing of the pH. The E_{pit} of samples in acid solution and neutral solution under the same deformation didn't have big difference; however, there was a high promotion in alkaline solutions. The appearance of the polarization curves in the alkaline solution was much different of that in acid and neutral chloride solution, which might also result from the different corrosion mechanism.

The cathodic reactions possibly occurred in acid and neutral chloride solution, as the following Eqs:

$$2H^+ + 2e^- \rightarrow H_2\uparrow \quad (2)$$
$$2H_2O + 2e^- \rightarrow 2OH^- + H_2 \quad (3)$$
$$O_2 + 2H_2O + 4e^- \rightarrow 4OH^- \quad (4)$$
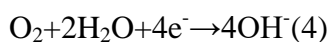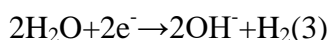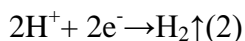
The anodic reactions are mainly the iron dissolution, and other alloys dissolution, as Eq.5:

$$M \rightarrow M^{2+} + 2e^- \text{ (M replaces Fe, Cr, Ni)} \quad (5)$$

In the alkaline solutions the curves were different from the curves correspond to neutral solution and acid solution. The current gently increased at 700 mV vs. SCE instead of increasing rapidly in the neutral solution or acid solution. This may be due to the transpassivation reaction of the samples correspond to the reaction, as Eq.6:

$$4OH^- \rightarrow 2H_2O + O_2 + 4e^- \quad (6)$$
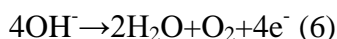
However, when the potential increased around 800 mV, the current density increased rapidly. When the potentiodynamic polarization curves was terminated at 700mV, the pits could not be observed under the optical microscope. Observation results showed that the pitting corrosion took place in the period of rapid current growth. Nevertheless, the current increased slightly around at 300mV vs. SCE. The reason was that insoluble passive film started to dissolve corresponding to the reaction, as Eq7;

$$Cr_2O_3 + OH^- \rightarrow 5H_2O + 2CrO_4^{2-} + 6e^- \quad (7)$$

Therefore, there was no breakdown of the passive layer in the reaction (5), the pitting corrosion occurred in reaction (6) when potential was around 800mV because of the dissolution of the film-. This explained why the E_{pit} of samples were similar in acidic and neutral solution while the E_{pit} of samples were greatly improved in alkaline solution. In addition, the E_{pit} of samples under different deformation

in alkaline solution were dispersed compared with that in neutral or acid solution, this may be due to the E_{pit} obtained by the potentiodynamic polarization curve measurement was unique, even with a great randomness. Meanwhile, the passivation current had no obvious change in different pH solutions which meant the passivation of UNS S32205 DSS was hardly affected by the SIM.

In the end, the corrosion potential of 30% deformed specimens was -359mV the same as the specimen under the strain deformation on 20%, lower than that of other deformed specimens which might be attributed to the high dislocation density in strain induced by α'-martensite.

Some authors reported corresponding investigations in this field. Wang et al. [28] found that the film generated in the alkaline solution was greater in intensity and thickness, so as to inhibit pitting corrosion. This is due to a relatively thick and compact passive film formed in an alkaline solution as result of preventing efficiently the matrix metal from being affected by the solution. Prawoto et al. [29] found that the UNS S32205 corrosion rate increased with the decreasing of pH. Albrimi et al. [30] concentrated on austenitic stainless and found the corrosion sensitivity increase with the increase of hydrogen ion concentration in media containing chloride ions. Loto et al. [31] focused on ferritic stainless steel and found the corrosion rate of stainless steel was affected by the pH. Leban et al. [32] studied the deformation-induced martensite of AISI 321 and found that the martensite could cause the initiation of pitting corrosion. In agreement with the works mentioned above, it is found that the corrosion resistance of UNS S32205 was affected by the SIM. The corrosion potential of martensitic is lower than the austenite and ferrite. Therefore, the martensitic is more susceptible to pitting corrosion than other phases in the duplex stainless steel. Moreover, we found that the amount of SIM increased with the increasing of the strain deformation, the strain duplex stainless steel was more sensitive to pitting corrosion in acid chloride solution.

4. CONCLUSIONS

In this paper, the effects of plastic deformation and SIM in a UNS S32205 DSS were investigated. Conclusion can be drawn as followed:

1.   The sequence of martensitic transformations in UNS S32205 DSS was γ →α'. The amount of SIM increased with the increasing of the strain deformation.

2.   The Vickers micro-hardness increased linearly from 240 to 337 with the increase of the strain, and the magnetization saturation increased monotonically, which arises from the transformation of the induced plasticity.

3.   The pitting potential decreased in acid chloride solution at pH≈2 (3.5 wt.% NaCl+0.01 mol/L HCl) with the increase of the deformation, however, in 3.5 wt.% NaCl solution and pH≈12 (3.5 wt.% NaCl+0.01 mol/L NaOH), the pitting corrosion was hardly effected by the SIM.

4.   The pitting corrosion of UNS S32205 DSS occurred on the activation area in the acid (3.5 wt.% NaCl+0.01 mol/L HCl) and neutral (3.5 wt.% NaCl) solutions, while the pitting corrosion occurred in the transpassivation area in the alkaline (3.5 wt.% NaCl+0.01 mol/L NaOH) solution.

References

1. J.O. Nilsson, *Mater. Sci. Tech.-Lond.*, 8 (1992) 685-700.
2. J.O. Nilsson, A. Wilson, *Mater. Sci. Tech.-Lond.*, 9 (1993) 545-554.
3. C. Blawert, A. Weisheit, B.L. Mordike, F.M. Knoop, *Surf. Coat. Tech.*, 85 (1996) 15-27.
4. J. Charles, *Steel Res. Int.*, 79 (2008) 455-465.
5. S.M. Wessman, S. Hertzman, R. Pettersson, R. Lagneborg, M. Liljas, *Mater. Sci. Tech.-Lond.*, 24 (2008) 348-355.
6. J. Gong, Y.M. Jiang, B. Deng, J.L. Xu, J.P. Hu, J. Li, *Electrochim. Acta*, 55 (2010) 5077-5083.
7. W. Zhang, L. Jiang, J. Hu, H. Song, *Mater. Charact.*, 60 (2009) 50-55.
8. L. Zhang, W. Zhang, Y. Jiang, B. Deng, D. Sun, J. Li, *Electrochim. Acta*, 54 (2009) 5387-5392.
9. I. Altenberger, B. Scholtes, U. Martin, H. Oettel, *Mat. Sci. Eng. A-Struct.*, 264 (1999) 1-16.
10. W. Hubner, *Tribol. Int.*, 34 (2001) 231-236.
11. G. Frommeyer, U. Brux, P. Neumann, *Isij Int.*, 43 (2003) 438-446.
12. H.F.G.D. Abreu, S.S.D. Carvalho, P.D. Lima Neto, R.P.D. Santos, V.N. Freire, P.M.D.O. Silva, S.S.M. Tavares, *Materials Research*, 10 (2007) 359-366.
13. A. Weisbrodt-Reisch, M. Brummer, B. Hadler, B. Wolbank, E.A. Werner, *Mat. Sci. Eng. A-Struct.*, 416 (2006) 1-10.
14. B. Soylu, R. Honeycombe, *Mater. Sci. Tech.-Lond.*, 7 (1991) 137-145.
15. C. Herrera, D. Ponge, D. Raabe, *Acta Mater.*, 59 (2011) 4653-4664.
16. M. Breda, K. Brunelli, F. Grazzi, A. Scherillo, I. Calliari, *Metall. Mater. Trans. A*, 46A (2015) 577-586.
17. Y. Guo, J. Hu, Y. Jiang, J. Li, *Int. J. Electrochem. Sc.*, 11 (2016) 4812-4827.
18. R.E. Schramm, R.P. Reed, *Metall. Trans. A*, 6 (1975) 1345-1351.
19. S. Pramanik, S. Bera, S.K. Ghosh, *Steel Res. Int.*, 85 (2014) 776-783.
20. W.T. Tsai, I.H. Lo, *Corrosion*, 64 (2008) 155-163.
21. S.M. Alvarez, A. Bautista, F. Velasco, *Corros. Sci.*, 53 (2011) 1748-1755.
22. A. Kashiwar, N.P. Vennela, S.L. Kamath, R.K. Khatirkar, *Mater. Charact.*, 74 (2012) 55-63.
23. H. Ha, M. Jang, T. Lee, J. Moon, *Corros. Sci.*, 89 (2014) 154-162.
24. W.J. Babyak, F.N. Rhines, *Trans. Am. Inst. Min. Metall. Eng.*, 218 (1960) 21-23.
25. G.B. Olson, M. Cohen, *Metall. Trans. A*, 6 (1975) 791-795.
26. S. Allain, J.P. Chateau, O. Bouaziz, *Mat. Sci. Eng. A-Struct.*, 387 (2004) 143-147.
27. R.T. Loto, C.A. Loto, Int. *J. Electrochem. Sc.*, 7 (2012) 9423-9440
28. Y. Wang, G. Cheng, W. Wu, Q. Qiao, Y. Li, X. Li, *Appl. Surf. Sci.*, 349 (2015) 746-756.
29. Y. Prawoto, K. Ibrahim, W.B.W. Nik, Arab. *J. Sci. Eng.*, 34 (2009) 115-127.
30. Y.A. Albrimi, A. Eddib, J. Douch, Y. Berghoute, M. Hamdani, R.M. Souto, *Int. J. Electrochem. Sc.*, 6 (2011) 4614-4627.
31. C.A. Loto, R.T. Loto, *Int. J. Electrochem. Sc.*, 7 (2012) 11011-11022.
32. M.B. Leban, R. Tisu, *Eng. Fail. Anal.*, 33 (2013) 430-438.